A synthetic route for the effective preparation of metal alloy nanoparticles and their use as active electrocatalysts

Rodriguez, Paramaconi; Monzo Gimenez, Francisco Javier; Bennett, Elizabeth; Humphrey, Jo ; Plana, Daniela; Walker, Marc ; McConville, Christopher; Fermin, David

DOI:
10.1021/acscatal.5b02598

Document Version
Peer reviewed version

Citation for published version (Harvard):
Rodriguez, P, Monzo Gimenez, FJ, Bennett, E, Humphrey, J, Plana, D, Walker, M, McConville, C & Fermin, D 2016, 'A synthetic route for the effective preparation of metal alloy nanoparticles and their use as active electrocatalysts', *ACS Catalysis*, vol. 6, no. 3, pp. 1533-1539. https://doi.org/10.1021/acscatal.5b02598

A Synthetic Route for an Effective Preparation of Metal Alloy Nanoparticles and Its Use as Active Electrocatalyst

Elizabeth Bennett[a], Javier Monzó[a], Jo Humphrey[b], Daniela Plana[b], Marc Walker[c], Christopher McConville[c], David Fermin[b], Alex Yanson[d] and Paramaconi Rodriguez[a]*

[a]School of Chemistry, University of Birmingham, Edgbaston, B15 2TT, UK.

B School of Chemistry, University of Bristol, Cantocks Close, Bristol, BS8 1TS,UK

[c]Department of Physics, University of Warwick, Coventry, CV4 7AL, UK.

[d]Cosine Measurement Systems, Oosteinde 36, 2361 HE Leiden. The Netherlands

*Corresponding author: P.B.Rodriguez@bham.ac.uk.

Abstract

By taking advantage of the non-equilibrium synthetic conditions, the cathodic corrosion method was used to prepare a selected a number of alloys of which solid-solution alloys do not exist under ambient conditions. To illustrate our finding we present the preparation at room temperature of PtBi and PtPb alloy nanoparticles with various compositions. These alloys have shown benchmark mass activity and durability towards the formic acid oxidation. The improvement in the catalytic activity is explained based on the composition of the metal alloys, the reduced particle size and, quite importantly, the level of cleanliness of the catalyst obtained by this method.

Visual Abstract

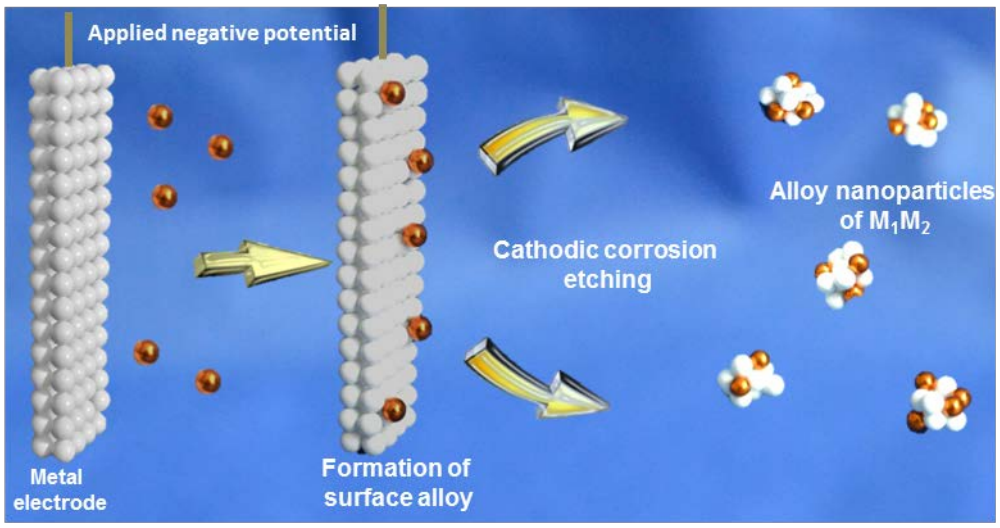

Keywords: Alloy nanoparticles, PtBi, PtPb, formic acid oxidation, cathodic corrosion.

The synthesis of metal alloy and mixed oxide nanoparticles is one of the most widely investigated topics in materials science[1-5]. These materials are without doubt one of the pillars in the technological development of society and nowadays are taking a leading role in the development of green sources of energy in fuel cells[3, 6-8], Li batteries[9], photocatalysts[10] and other applications [11, 12].

In the process of developing new alloy nanocatalysts, special attention has been paid to improving physical properties by controlling composition, size and structure, since these properties are the key to improved selectivity and enhanced activity[2, 4, 13-16]. Among these properties, the composition of the alloys is perhaps the most important parameter since the chemical and physical properties of the alloy are correlated with the electronic states. Unfortunately, a large number of metals are immiscible with each other under ambient conditions and in a wide range of temperatures; other metal combinations have large miscibility gaps in the bulk form [17, 18] and therefore metallurgical high temperature methods are traditionally needed to prepare bimetallic alloys, involving melting of two bulk metals.[24,25] Other similar methods have been reported in the

literature such as laser ablation[19, 20], induction melting[26] and microwave synthesis[27]; these methods often use high temperatures of near or greater than 1000 °C[28] for long periods of time and are therefore inefficient. Temperatures of above 600 °C are known to cause sintering of particles, thereby increasing the particle size and reducing the surface area and number of accessible active sites.[21] In addition, and more importantly, scaling-up these processes for industrial applications is not straightforward and will require large investment.

Recently, Yanson et al. reported a new electrochemical method for the preparation of metal nanoparticles, the so-called "cathodic corrosion" [21, 22]. The method is based on the polarization of a metal electrode at sufficient negative potentials, enough to form cation-stabilized metal anions, which then act as intermediates for the formation of nanoparticles. The formation of these cation-stabilized metal anions species in water is possible due to the non-equilibrium conditions of the system at such negative potentials [22]. So far, the method has been proven to work not just for the synthesis of metal nanoparticles, but also for the synthesis of certain alloy nanoparticles when the precursor is a bulk alloy (e.g PtRh, PtNi, AuCu, etc) . More interestingly, the alloy nanoparticles produced by this method retained the composition of the starting alloy [21]. However, the methodology proposed until now required the utilization of the metal alloy as a starting material limiting its application for the synthesis of many other alloys not stable in bulk phase.

Herein we report the preparation of alloy nanoparticles using a modification of the cathodic corrosion method as illustrated in Figure 1A.[23] Such modification includes the utilization of the main metal as a bulk electrode material while the second metal for the final alloy is present in the electrolyte during the synthesis. The mechanism includes the formation of a surface alloy between the two main metals, subsequently followed by the formation of the metal alloy complex, anion-stabilized by the alkali cation present in solution.

To prove our concept we have selected a number of alloys of which solid-solution alloys do not exist in equilibrium in the bulk state. To illustrate our finding we will present the preparation of PtBi and PtPb alloy nanoparticles with various compositions. It has been extensively described in the literature by the groups of Abruña and Di Salvo that PtBi and $PtBi_2$ intermetallics show increased catalytic activity at lower onset potentials toward the oxidation of formic acid [23-25]. Compared with methanol, formic acid is an excellent candidate for low temperature fuel cells due to its relative non-toxicity and low fuel crossover.[5] More recently, a study from Ji et al. showed a synthesis method capable of producing intermetallic PtBi nanoparticles of 1-3 nm in diameter, overcoming the problem of particle size [26]. In an attempt to control the shape, Liao et al. reported the synthesis of PtBi intermetallics with particle size of 20-100 nm with certain preferential surface structures[27]. However in all the above cases, three main common drawbacks can be distinguished: i) the utilization of expensive organic precursors; ii) the high temperatures and iii) the time of synthesis (including cleaning protocols). Similar finding regarding the catalytic activity towards the formic acid oxidation have been reported for PtPb intermetallics and alloy nanoparticles.[25, 28, 29] The synthesis method for those is similar and presents the same drawbacks.

By following the modified cathodic corrosion method as described in Figure 1, we were able to prepare PtBi and PtPb nanoparticles with different metal compositions in the range between 60 % to 5 % Pt (See experimental section for more details). Figure 1B and Figure 1C show the Transmission Electron Microscopy (TEM) images and particle size distribution of the $Pt_{70}Bi_{30}$ and $Pt_{90}Pb_{10}$ nanoparticles prepared by the cathodic corrosion method. The images show a homogeneous particle size distribution of the alloy nanoparticles. On counting over a thousand particles, the average particle size of the $Pt_{70}Bi_{30}$ alloy was found to be 5.3 nm ± 1.2 nm, whereas the diameter of the $Pt_{90}Pb_{10}$ particles were found to be slightly smaller, 4.2 nm ± 0.7 nm.

The bulk composition of the alloy nanoparticles was determined by Energy-Dispersive X-ray spectrocopy (EDX) and X-Ray fluorescence (XRF), as exemplified in Figure 2. Figure 2A shows characteristic XRF peaks of PtBi and PtPb nanoparticles, where peaks at 8.27, 9.45, 11.09 and 11.25 keV correspond to platinum; 10.85, 13.07 and 15.28 keV are associated with the presence of bismuth, and the lines associated with lead appear at 10.58 and 12.61 keV. Figure 2B shows a typical EDX analysis obtained for PtBi and PtPb nanoparticles with characteristic peaks of M Bismuth (2.41 keV), M Pb (2.35 keV) and M Pt (2.05 keV). The software used to analyse the EDX spectra corrects standard artefacts such as the spectrum background and the effect of close peaks. The EDX analysis showed slightly higher values of Bi and Pb than XRF analysis, which may be associated with the thickness of the sample layers. Further aspects related to composition were examined by X-ray photoelectron spectroscopy (XPS) as shown in Figure 3. This figure shows the core level spectra acquired from the Pt 4f, Bi 4f, Pb 4f and O 1s energy levels in the $Pt_{70}Bi_{30}$ and $Pt_{90}Pb_{10}$ nanoparticles. In order to make an appropriate comparison, the XPS spectra of Pt nanoparticles prepared under the same experimental conditions is included in the figure (full characterization of the Pt nanoparticles is provided in Figure S1). Focusing on the PtBi alloy, the features observed at 74.18 eV and 71.35 eV arise from the Pt $4f_{5/2}$ and Pt $4f_{7/2}$ components from the Pt-Bi bonding environment. However the band associated with the Pt $4f_{5/2}$ is slightly shifted in comparison with the values of the bare platinum nanoparticles (74.45 eV) and reference values in the literature[30]. This shift in the Pt $4f_{5/2}$ could be attributed to the interaction with more electronegative species. However this shift could be associated with other parameters, as will be explained below. The XPS spectra also confirm the existence of Pt bulk oxide species[30] by the appearance of a component at 78.14 eV, which is also shifted toward higher binding energies when compared with the Pt nanoparticles. The Bi 4f spectrum presents two distinct features at 159.8 eV (Bi $4f_{7/2}$), and 165.1 (Bi $4f_{5/2}$)[31](Figure S2). These bands indicate the presence of highly oxidized bismuth species (e.g. $BiO(OH)$[31]). The peaks located at 158 eV and 163 eV are located at

slightly higher binding energy than the characteristic signal associated with Bi-Bi bond (i.e. 157 eV and 162 eV). This shift can be attributed to the charge displacement originating from Pt-Bi bonding. Similar results have been reported for Pt single-crystals decorated with irreversibly adsorbed bismuth.[32]

In the case of PtPb nanoparticles, the line of the XPS signal for the Pt $4f_{5/2}$ on the PtPb nanoparticles is shifted towards lower binding energy when compared with the Pt nanoparticles. In addition, and contrary to the observation for PtBi, the XPS also confirms the absence of surface Pt oxide species. Analysis of the Pb 4f region reveals components located at 137.5 and 138.9 eV ($4f_{7/2}$), and 142.2 and 143.5 eV ($4f_{5/2}$) (Figure S2). Here, the lower energy bonding environment (137.5 eV and 142.2 eV) is ascribed to Pt-Pb bonding, while the higher energy pair of components are due to highly oxidised Pb states. As in the case of bismuth, the relative intensity of the higher energy component suggests that a large fraction of the lead present in the near-surface region is in the oxidized form[33]. The binding energies of oxygen in the bismuth alloys and the lead alloys are significantly different. While in the case of bismuth alloy we should consider the formation of PtBi oxides, several oxidized species including PbO, $Pb(OH)_2$ and $PbCO_3$ can be found on air-exposed samples of lead alloys, as reported previously[33]. The absence of the Pt bulk oxides on the PtPb samples can be attributed to preferred formation of the Pb oxides over the formation of Pt bulk oxides[33]. However, the presence of atmospheric contaminants (H_2O, CO, etc) makes analysis of the O 1s region more complex. Given that the analysis of oxide species in the Pt, Pb and Bi core levels is more clear-cut, detailed analysis of the O 1s region is not required in order to fully examine the metal oxide species present at the nanoparticle surface. It is also important considering that particle size and lattice strain can affect the separation of the Pt $4f_{5/2}$ and $4f_{7/2}$ doublets as well as differences in oxide content(?).[34-36]

The composition of the alloy nanoparticles can be controlled not only by changing the composition of the solution (e.g. concentration of one of the metals), but also by changing the synthesis parameters, such as amplitude and offset. In this regard, we have prepared a range of PtBi and PtPb nanoparticles with different compositions (Figure S3 and S4).

Following physical characterisation, the electrochemical characterization and the electrochemical activity towards the formic acid oxidation in acidic media were assessed. The voltammetric profiles of the $Pt_{70}Bi_{30}$ and $Pt_{90}Pb_{10}$ nanoparticles in 0.5 M H_2SO_4 solution are shown in Figure 4A and 4B. The voltammetric profile of the pure platinum nanoparticles prepared under the same conditions and with similar particle size is included for the sake of comparison. The voltammograms are presented in current density per mass since the total loading of the catalyst on the electrode was the same in the three cases (12.75 mg/ cm^2). As can be seen, the region between 0.06 and 0.5 V vs RHE, associated with the hydrogen adsorption/desorption process, is suppressed due to the decrease in the number of free Pt sites on the surface. In the case of the $Pt_{70}Bi_{30}$ alloy, the voltammetric profile shows a current contribution at around 0.8-0.9 V, associated with the redox behaviour of Bi at the surface[33, 37, 38].

Figures 4C and 4D show the voltammetric profiles of the $Pt_{70}Bi_{30}$ and $Pt_{90}Pb_{10}$ nanoparticles in acidic media in presence of formic acid. In this case, in order to make an appropriate comparison of the mass activity, the results are presented also in current density per mass of catalyst. From the voltammetric profiles, it can be seen that the onset in the formic acid oxidation on $Pt_{70}Bi_{30}$ nanoparticles appears around 0.1 V vs RHE, while the onset of the formic acid oxidation on $Pt_{90}Pb_{10}$ occurs at a slightly more positive potential (0.2 V vs RHE). The onset potentials observed in this work were comparable to the lowest achieved in similar systems employing PtBi intermetallics[23, 26], PtPb alloys/intermetallics[28, 29] , PtPd alloys[39] and Pt single crystal electrodes surface modified with Bi[40]. Regarding the mass activity, both catalysts present current densities

two orders of magnitude higher than that of pure Pt. The mass activity at 0.3 V (the typical anodic working voltage in Direct Formic Acid Fuel Cell (DFAFC))[41] in both of our catalysts $Pt_{70}Bi_{30}$ (630 mA/mg) and $Pt_{90}Pb_{10}$ (800 mA/mg) significantly exceeds the values of the state-of-the-art catalysts reported in the literature[26].

Even more interesting is the absence of hysteresis between the positive and the negative scan when the potential is cycled between 0.06 and 1 V (Figure S5 and S6). This is a clear indication that the PtBi and PtPb follow the direct pathway in the oxidation of formic acid to CO_2[42]. In order to confirm that, CO_2 formation was determined by following the signal at m/z=44 of the On-Line Electrochemical Mass Spectrometer (OLEMS). Figures 4E and 4F show how the onset in the formation of CO_2 correlates with the onset in the cyclic voltammetries in Figures 4C and 4D.

The long term durability is always the determining parameter when evaluating a catalyst for DFAFC or similar devices[41, 43]. Therefore the performance of the $Pt_{70}Bi_{30}$ and $Pt_{90}Pb_{10}$ nanoparticles was evaluated by chronoamperometric measurements at 0.3 V. As can be seen in Figure 5, the initial activity of the $Pt_{70}Bi_{30}$ exceeds the catalytic activity of both Pt and $Pt_{90}Pb_{10}$ nanoparticles. However, this catalyst suffers rapid performance decay over time. On the other hand, the $Pt_{90}Pb_{10}$ shows steady state currents during the whole experiment, confirming its improved stability. The currents recorded at 60 minutes for the oxidation of formic acid on the $Pt_{90}Pb_{10}$ alloy nanoparticles (391 mA/mg) surpass the performance, under similar conditions, of catalysts reported by Ji et al.[26] (220 mA/mg PtBi) and Liao et al (120 mA/mg PtBi)[27] by more than 70 %.

In conclusion, we have described a single pot, room temperature method for the preparation of solid-solution alloy nanoparticles, the constituent elements of which are immiscible in the bulk state at room temperature. This novel method takes advantage of the non-equilibrium synthetic conditions of cathodic corrosion. To demonstrate the efficiency of the method we have showed the preparation of binary PtBi and PtPb nanoparticles with different compositions. These

nanoparticles were homogeneously dispersed and exhibited extraordinary activity towards formic acid oxidation. Although the oxidation of formic acid has been extensively studied in recent decades due to its enormous importance in the fuel cell technology (DFAFC and as an intermediate in methanol oxidation for DAFC)[44-47], herein we reported catalyst compositions of $Pt_{70}Bi_{30}$ and $Pt_{90}Pb_{10}$ with significant enhancements of activity and durability. The improvement in the catalytic activity in comparison with previous systems could be attributed not just to the composition of the metal alloys, but also to the reduced particle size and, quite importantly, the level of cleanness of the catalyst. The method is not limited just to the formation of PtBi and PtPb. We have also been able to prepare $Pt_{65}Sn_{30}$ nanoparticles which showed enhanced catalytic properties towards the ethanol oxidation in acidic media (Figure S7). The application of the method for the preparation of alloy nanoparticles was extended to other metals, e.g. $Pd_{60}Pb_{40}$ and $Au_{85}Cu_{15}$ alloys (Figure S8)

It is important to note the "green" character of this synthetic method, since it does not require organic ligands, capping agents, nor high temperatures, and therefore the catalytic activity will not be affected by undesirable adsorbed species. Other benefits of the method include the suitability for scale up for industrial applications, avoiding large investments in large volumes of organic solvents, heating or cleaning treatment, and incurred safety and disposal issues.

Finally, the time of synthesis of the catalyst is an important parameter to consider for further industrial applications. While the synthesis procedures described before [24-27] take 12-24 hours of synthesis (excluding cleaning protocols), the cathodic corrosion method is capable of producing a high yield of nanocatalyst in a few minutes (Figure S9), and long and tedious cleaning procedures are not required to obtain clean catalysts.

Finally, the cathodic corrosion method has demonstrated unparalleled control over size and shape of metal nanoparticles[48]. There is every reason to believe that shape-controlled alloy nanoparticles will perform even better as catalysts for fuel cells[2, 49].

Experimental Methods

Synthesis of PtBi and PtPb nanoparticles

A mixture of 50:50 saturated calcium chloride and MilliQ water (18.2 MΩ cm, 1 ppb total organic carbon) was used to prepare the catalysts. Clean nanoparticles were prepared following a modified version of the cathodic corrosion method[23,15] as described in Figure 1A, in which a Pt wire (diameter 0.125 mm, 99.999% Alfa Aesar) was submerged into 10 ml of a $CaCl_2$ solution containing either Bi_2O_3 (saturated in 0.1 M $HClO_4$) or $PbCO_3$ (10^{-5} M in 0.01 M $HClO_4$) to prepare the PtBi or PtPb nanoparticles, respectively. A square wave voltage between -10 – 0 V was applied between the platinum working electrode and the platinum counter electrode. In order to keep the concentration of the second metal constant near to the working electrode and obtain homogenous composition of the nanoparticles the working electrode (Pt wire) was rotated at 50 RPM using a homemade holder and a Pine Instruments RDE. The rotation also allows the removal of hydrogen bubbles from the electrode, thereby preventing drops in conductivity. Following complete corrosion of the platinum wire, the resulting suspension was cleaned by centrifuging, decanting and re-dispersing in more MilliQ water until the excess reactants had been removed.

Characterisation

X-ray diffraction patterns were collected at an angle range of 20 – 110° in 2θ on a Bruker D2 PHASER powder X-ray diffractometer operating at 30 kV and 10 mA and fitted with a Co tube.

The X-ray photoemission spectroscopy (XPS) data were collected at the University of Warwick Photoemission Facility, more details of which are available[50]. For XPS analysis the samples were deposited on conductive silicon wafers. The samples investigated in this study were mounted on Omicron sample plates using electrically conductive carbon tape and loaded into the fast-entry chamber. Once a pressure of less than 1 x 10^{-7} mbar had been achieved (approx. 1 hour), the

samples were transferred to a 12-stage storage carousel, located between the preparation and main analysis chambers, for storage at pressures of less than 2 x 10^{-10} mbar.

XPS measurements were conducted in the main analysis chamber (base pressure 2 x 10^{-11} mbar), with the sample being illuminated using an XM1000 monochromatic Al Kα X-ray source (Omicron Nanotechnology). The measurements were conducted at room temperature and at a take-off angle of 90°. The photoelectrons were detected using a Sphera electron analyser (Omicron Nanotechnology), with the core levels recorded using a pass energy of 10 eV (resolution approx. 0.47 eV). The data were analysed using the CasaXPS package, using Shirley backgrounds, mixed Gaussian-Lorentzian (Voigt) line shapes and asymmetry parameters where appropriate. All binding energies were calibrated using the Fermi edge of a polycrystalline Ag sample, measured immediately prior to commencing the measurements.

TEM images were carried out on a JEM-2100. Ethanol suspensions of each catalyst were drop-casted on carbon-coated copper grids and then air-dried to create the resulting samples. EDX spectra were performed on a JEOL 2100 SEM. XRF analyses were run on an S8 TIGER.

General cleaning procedure, electrode preparation and electrochemical analysis

Glassware was soaked overnight in a potassium permanganate solution; this was then removed with a 3:1 solution of H_2O_2 and H_2SO_4 and finally rinsed with MilliQ water. This method was used prior to experiments in order to remove contaminants. Suprapur (Merck) reagents and MilliQ water (resistivity >18.2 MΩ cm) were used to prepare solutions and argon gas (6N, BOC) was bubbled into these before measurements to purge oxygen.

The working electrode was prepared by drop casting 22.5 μL of the suspension of nanoparticles in water onto a glassy carbon Rotating Disk Electrode (RDE). The total loading of the nanoparticles in every experiment was 12.75±0.15 g/ cm^2. Different models of Autolab potentiostats were used

and a Modulated Speed Rotator from Pine was used to control the rotation rate during the electrochemical measurements. A high surface area gold wire was used as counter electrode and reversible hydrogen electrode was used as reference. The counter electrode was flame annealed before to remove traces of organics. All measurements were performed at room temperature. The formic acid solutions were prepared with formic acid (98%, VWR)

On-Line electrochemical Mass Spectrometry (OLEMS)

Online Electrochemical Mass Spectrometry (OLEMS) was used to detect the gaseous products formed during the reaction. The home built OLEMS setup consists of two differentially pumped chambers divided by a gate vale and a conical pinhole of 2mm diameter and a quadrupole mass spectrometer[51]. The two chambers were pumped by two Pfeiffer HiPace 80 (65 L s^{-1}) turbo molecular pumps, both backed in parallel by a Pfeiffer ACP 15, Standard, three phase, manual gas ballast, in order to avoid contamination from oil vapours. The turbo molecular pump at the analysis chamber was set up at the 80% of its pumping rate capacity (10^{-8}-10^{-9} mbar), while the pump at the collection chamber was set at 40% of its pumping capacity (10^{-4}-10^{-5} mbar). The quadrupole mass spectrometer was a PrismaPlus Compact mass spectrometer mass range: 1-200 amu. The time constant of the mass spectrometer was in the millisecond regime, determined by the CO stripping voltammetry from a Pt(111) electrode in 0.5 M sulphuric acid at different scan rates between 1 mV-20 mV/s. The reaction products at the electrode interface were collected with a small tip positioned close to the electrode. The tip is a 1 mm diameter porous Teflon cylinder (Porex with an average pore size of 0.5 µm - 1 µm and 45 % - 55 % porosity) in a Kel-F holder. The tip configurations were cleaned overnight in a solution of 2 M NaOH solution (VWR, EMSURE) and rinsed 5 times with hot MilliQ water before use. An SEM accelerating voltage of 2100 V was used. The pressure was equilibrated for 1 h prior to each measurement.

Acknowledgements

PR would like to acknowledge the University of Birmingham for the financial support through the Birmingham fellowship program. EB and JM acknowledge the University of Birmingham for the financial support through PhD scholarships at the School of Chemistry. The University of Warwick Photoemission Facility used in this research was funded through the Science Cities Advanced Materials Project 1: Creating and Characterising Next Generation of Advanced Materials with support from AWM and ERDF funds. JH is grateful to NERC (DTP grant) and Sasol Technology UK Ltd for their financial support. DP and DJF acknowledge the EPSRC support through the programme EP/K007025/1. Some of the TEM studies were carried out in the Chemistry Imaging Facility at the University of Bristol with equipment partly funded by EPSRC (EP/K035746/1 and EP/M028216/1).

Supporting Information Available: Description of Contents. This material is available free of charge via the Internet at http://pubs.acs.org

References

1. **Clarke, J.K.A. Chem. Rev., 1975, 75, 291-305.**

2. **You, H.; Yang, S.; Ding, B.; Yang, H. Chem. Soc. Rev., 2013, 42, 2880-2904.**

3. **Baldizzone, C.; Mezzavilla, S.; Carvalho, H.W.P.; Meier, J.C.; Schuppert, A.K.; Heggen, M.; Galeano, C. ;Grunwaldt, J.-D. Schüth, F.; Mayrhofer, K.J.J. Angew. Chem. Int. Ed. 2014, 53, 14250-14254.**

4. **Xiong, S.; Qi, W.; Huang, B.;Wang, M. ChemPhysChem, 2011, 12, 1317-1324.**

5. **Ferrando, R.; Jellinek, J.; Johnston, R.L Chem. Rev., 2008, 108, 845-910.**

6. **Stamenkovic, V.R. ; Mun, B.S. ; Arenz, M. ; Mayrhofer, K.J.J ; Lucas, C.A.;G. Wang, G. ; Ross, P.N. ; Markovic, N.M. Nat. Mater., 2007, 6, 241-247.**

7. **Wang, Y.-J.; Zhao, N.; Fang, B.; Li, H.; Bi, X.T.; Wang, H. Chem. Rev., 2015, 115, 3433-3467.**

8. **Hu, G.; Nitze, F.; Gracia-Espino, E.; Ma, J.; Barzegar, H.R.; Sharifi, T.; Jia, X.; Shchukarev, A.; Lu, L.; Ma, C.; Yang, G.; Wågberg, T. Nat. Comm., 2014, 5, 5253.**

9. **Obrovac, M.N.; V. L. Chevrier, V.L. Chem. Rev., 2014, 114, 11444-11502.**

10. **Maeda, K.; Teramura, K.; Masuda, H.; Takata, T.; Saito, N.; Inoue, Y.; Domen, K. J.Phys.Chem. B, 2006, 110, 13107-13112.**

11. **Hamdou, B.; Gooth, J.; Böhnert, T.; Dorn, A.; Akinsinde, L.; Pippel, E.; Zierold, R.; Nielsch, K. Adv. Energy Mat., 2015, DOI: 10.1002/aenm.201500280.**

12. **Pei, Y.; LaLonde, A.D.; Heinz, N.A.; Snyder, G.J. Adv. Energy Mat., 2012, 2, 670-675.**

13. **Cui, C.; Gan, L.; Li, H.-H.; Yu, S.-H.; Heggen, M.; Strasser, P. Nano Lett., 2012, 12, 5885-5889.**

14. **Cui, C.; Gan, L.; Heggen, M.; Rudi, S.; Strasser, P. Nat. Mater, 2013, 12, 765-771.**

15. **Li, H.-H.; Cui, C.-H.; Zhao, S.; Yao, H.-B.; Gao, M.-R.; Fan, F.-J.; Yu, S.-H. Adv. Energy Mat., 2012, 2, 1182-1187.**

16. **Rawalekar,S.; Mokari,T. Adv. Energy Mat., 2013, 3, 12-27.**

17. **Okamoto, H. J. Phase Equilib., 1991, 12, 207-210.**

18. **Massalski, T.B.; Okamoto, H.; Subramanian, P. R.; Kacprzak, L., Binary Alloy Phase Diagrams, SM International, OH,USA, 1990.**

19. **Swiatkowska-Warkocka, Z.; Pyatenko, A.; Krok, F.; Jany, B.R.; Marszalek, M. Sci. Rep., 2015, 5, 9849.**

20. **Hagedorn, K.; Liu, B.; Marcinkevicius, A. J. Electrochem.Soc., 2013, 160, F106-F110.**

21. **Rodriguez, P.; Tichelaar,F.D.; Koper, M.T.M; Yanson, A.I. J. Am. Chem. Soc., 2011, 133, 17626-17629.**

22. **Yanson, A.I.; Rodriguez, P.; Garcia-Araez, N.; Mom, R.V.; Tichelaar, F.D.; Koper, M.T.M. Angew. Chem. Int. ., 2011, 50, 6346-6350.**

23. **Casado-Rivera, E.; Gál, Z.; Angelo, A.C.D.; Lind, C.; DiSalvo, F.J.; Abruña, H.D. ChemPhysChem, 2003, 4, 193-199.**

24. **Roychowdhury, C.; Matsumoto, F.; Mutolo, P.F.; Abruña, H.D.; DiSalvo, F.J. Chem. Mat., 2005, 17, 5871-5876.**

25. Roychowdhury, C.; Matsumoto, F.; Zeldovich, V.B.; Warren, S.C.; Mutolo, P.F.; Ballesteros, M.; Wiesner, U.; Abruña, H.D.; DiSalvo, F. J. Chem. Mater. 2006, 18, 3365-3372.

26. Ji, X.; Lee, K.T.; Holden, R.; Zhang, L.; Zhang, J.; Botton, G.A.; Couillard, M.; Nazar, L.F. Nat. Chem, 2010, 2, 286-293.

27. Liao, H.; Zhu, J.; Hou, Y. Nanoscale, 2014, 6, 1049-1055.

28. Kang, Y.; Qi, L.; Li, M.; Diaz, R.E.; Su, D.;Adzic, R.R.; Stach, E.; Li, J.; Murray, C.B. ACS Nano, 2012, 6, 2818-2825.

29. Matsumoto, F.; Roychowdhury, C.; DiSalvo, F.J.; Abruña, H.D. J. Electrochem. Soc., 2008, 155, B148-B154.

30. Parkinson, C.R.; Walker, M.; McConville, C.F. Surf. Sci., 2003, 545, 19-33.

31. Tripković, A.V.; Popović, K.D.; Stevanović, R.M.; Socha, R.; Kowal, A. Electrochem.Comm., 2006, 8, 1492-1498.

32. Hamm, U.W.; Kramer, D.; Zhai, R.S.; Kolb, D.M. Electrochim. Acta, 1998, 43, 2969-2978.

33. Blasini, D.R.; Rochefort, D.; Fachini, E.; Alden, L.R.; DiSalvo, F.J.; Cabrera, C.R.; Abruña, H.R. Surf. Sci., 2006, 600, 2670-2680.

34. Richter, B.; Kuhlenbeck, H.; Freund, H.J.; Bagus, P.S., Phys.Rev. Lett., 2004, 93, 026805.

35. Bagus, P.S.; Wieckowski, A.; Freund, H. Chem. Phys. Lett., 2006, 420, 42-46.

36. Lewera, A.; Zhou, W.P.; Hunger, R.; Jaegermann, W.; Wieckowski, A.; Yockel, S.; Bagus, P.S. Chem. Phys. Lett., 2007, 447, 39-43.

37. Clavilier, J.; Feliu, J.M.; Aldaz, A. J. Electroanal. Chem. Interfacial Electrochem., 1988, 243, 419-433.

38. Rodríguez, P.; Solla-Gullón, J.; Vidal-Iglesias, F.J.; Herrero, E.; Aldaz, A.; Feliu, J.M. Anal. Chem., 2005, 77, 5317-5323.

39. Lee, J.-Y.; Kwak, D.-H.; Lee, Y.-W.; Lee, S. Park, K.-W. Phys. Chem. Chem. Phys. 2015, 17, 8642-8648.

40. Chen, Q.-S.; Zhou, Z.-Y.; Vidal-Iglesias, F.J.; Solla-Gullon, J.; Feliu, J.M.; Sun, S.-G. J. Am. Chem. Soc., 2011, 133, 12930-12933.

41. Rice, C.; Ha, S.; Masel, R.I.; Waszczuk, P.; Wieckowski, A.; Barnard, T. J. Power Sources, 2002, 111, 83-89.

42. Macia, M.D.; Herrero, E.; Feliu, J.M. J. of Electroanal.Chem., 2003, 554-555, 25-34.

43. Yu, X.; Pickup, P.G. J. Power Sources, 2008, 182, 124-132.

44. Chen, Y.X.; Heinen, M.; Jusys, Z.;Behm, R.J. Langmuir, 2006, 22, 10399-10408.

45. Neurock, M.; Janik, M.; Wieckowski, A. Farad.Discuss., 2009, 140, 363-378.

46. Miki, A.;Ye, S.; Senzaki, T.; Osawa, M. J.of Electroanal.Chem., 2004, 563, 23-31.

47. Housmans, T.H.M.; Wonders, A.H.; Koper, M.T.M. J.Phys.Chem. B, 2006, 110, 10021-10031.

48. Duca, M.; Rodriguez, P.; Yanson, A.; Koper, M.T.M. Top. Catal., 2014, 57, 255-264.

49. Koenigsmann, C.; Santulli, A.C.; Gong, K.; Vukmirovic, M.B.; Zhou, W.-P.; Sutter, E.; Wong, S.S.; Adzic, R.R. J. Am. Chem. Soc., 2011, 133, 9783-9795.

50. S. http://go.warwick.ac.uk/XPS.

51. Monzo, J.; Malewski, Y.; Kortlever, R.; Vidal-Iglesias, F. J.; Solla-Gullon, J.; Koper, M. T. M.; Rodriguez, P. J. Mater. Chem. A 3, 23690-23698.

Figures

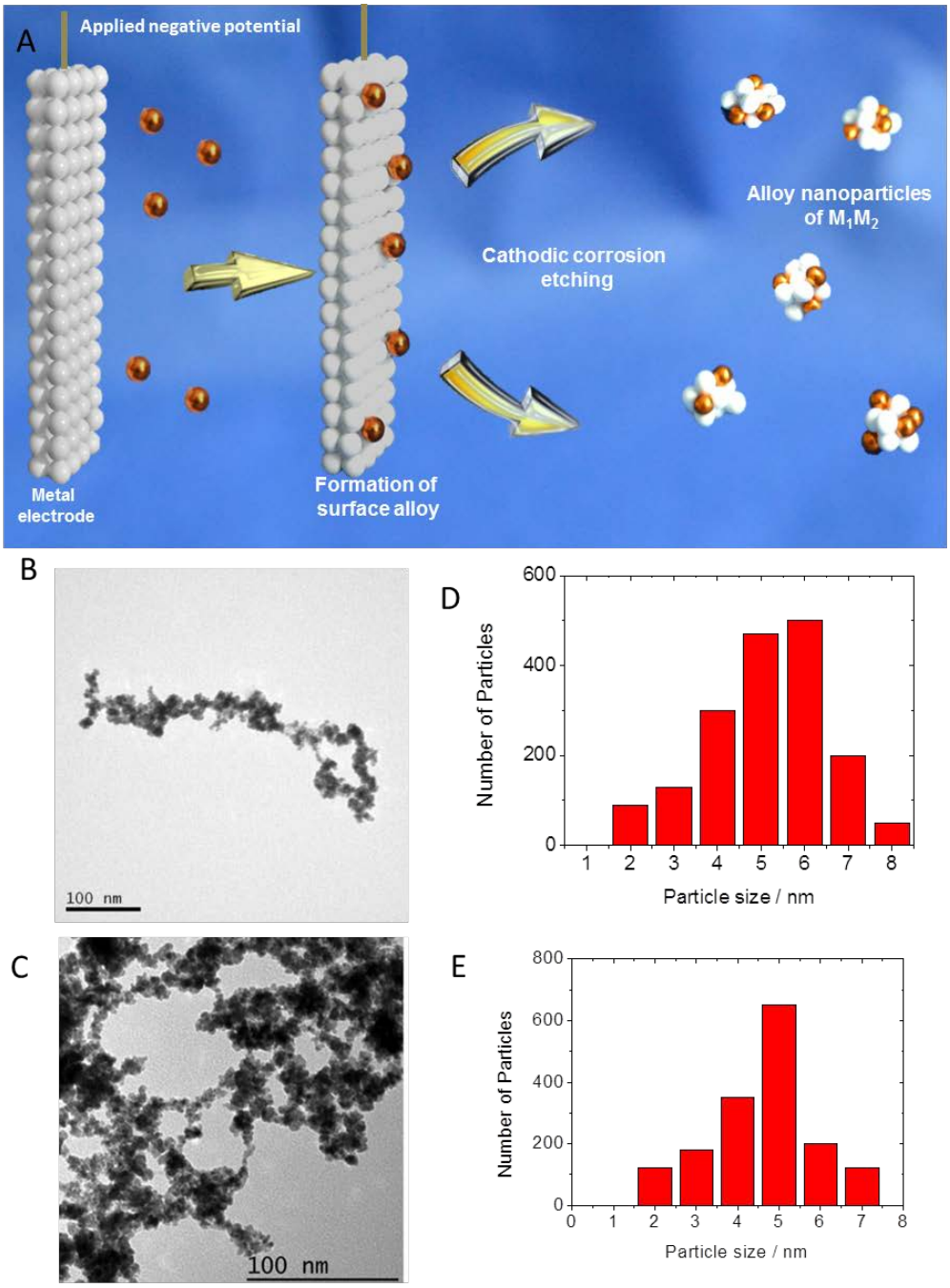

Figure 1. (A) Schematic representation of the cathodic corrosion reaction mechanism. TEM images of (B) $Pt_{90}Pb_{10}$ and (C) $Pt_{70}Bi_{30}$ nanoparticles and particle size distribution of (D)$Pt_{90}Pb_{10}$ and (E) $Pt_{70}Bi_{30}$ nanoparticles.

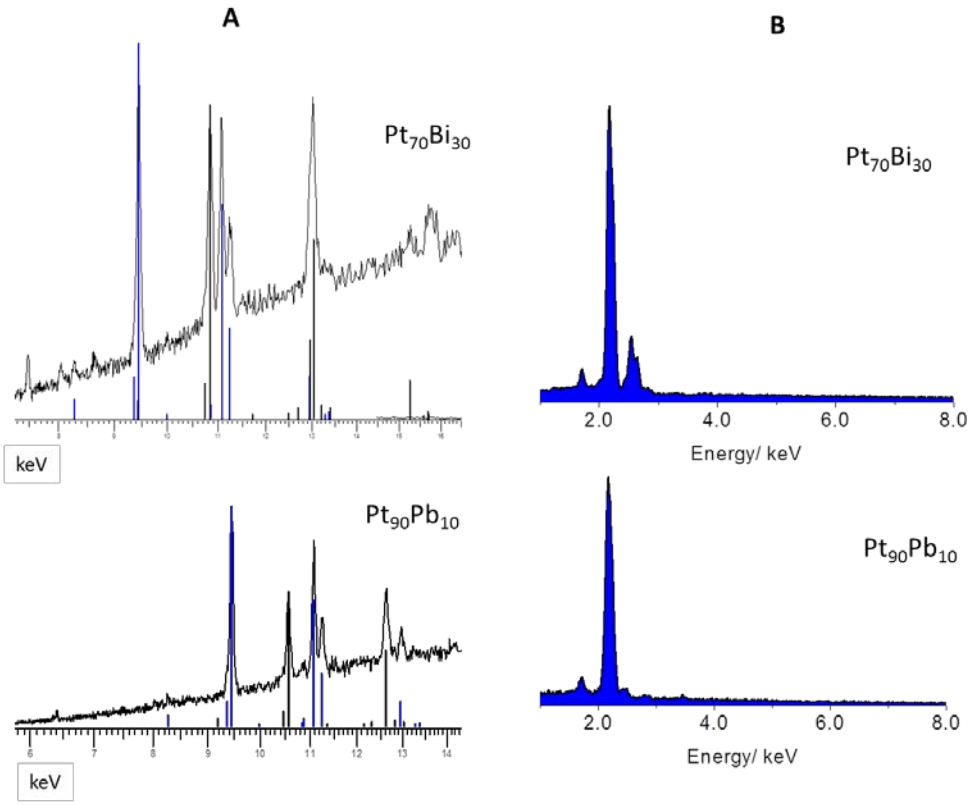

Figure 2. (A) XRF spectra and (B) EDX spectra of the of $Pt_{90}Pb_{10}$ and $Pt_{70}Bi_{30}$ nanoparticles. In the simulated XRF spectra for these alloys (thin vertical lines), blue lines represent Pt and black lines Pb and Bi, respectively.

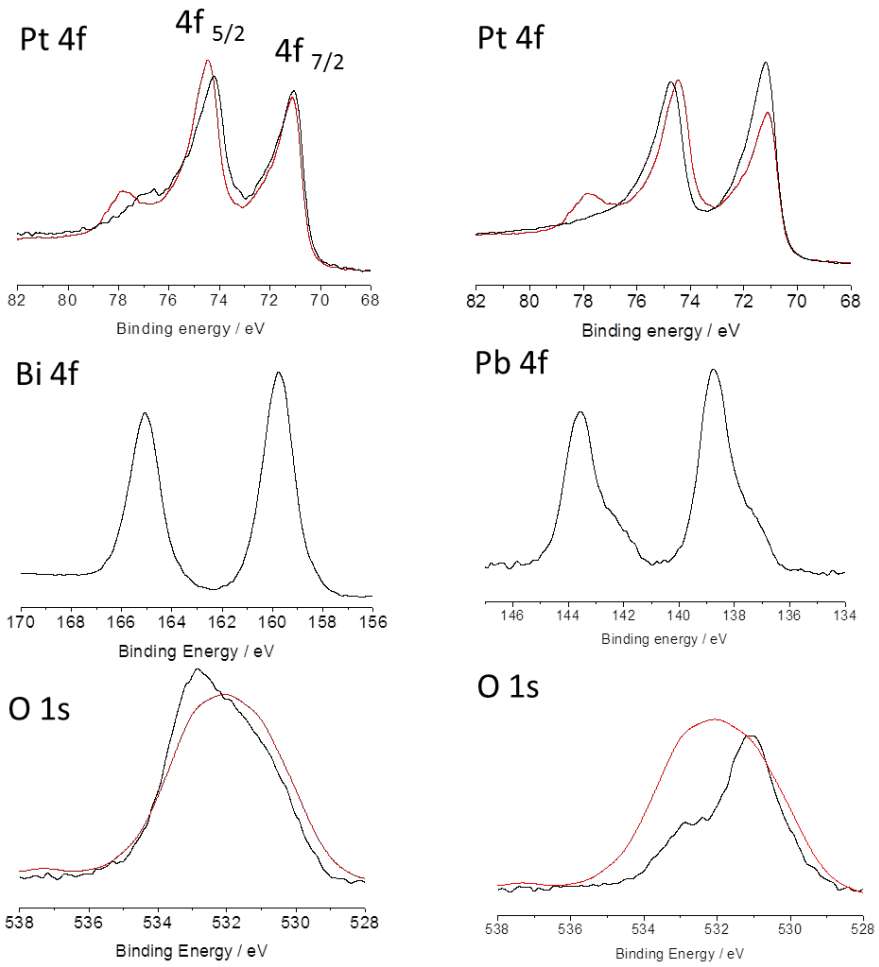

Figure 3. Core level XPS data from the Pt 4f, Bi 4f, Pb 4f and O 1s regions acquired from the surfaces of the $Pt_{70}Bi_{30}$ and $Pt_{90}Pb_{10}$ nanoparticles. The black curves in the left hand column were acquired from the $Pt_{70}Bi_{30}$ nanoparticles, whereas the corresponding data from the $Pt_{90}Pb_{10}$ nanoparticles are represented by the black curves in the right hand column. The red curves correspond to the Pt 4f and O 1s XPS lines for Pt nanoparticles prepared under the same experimental conditions.

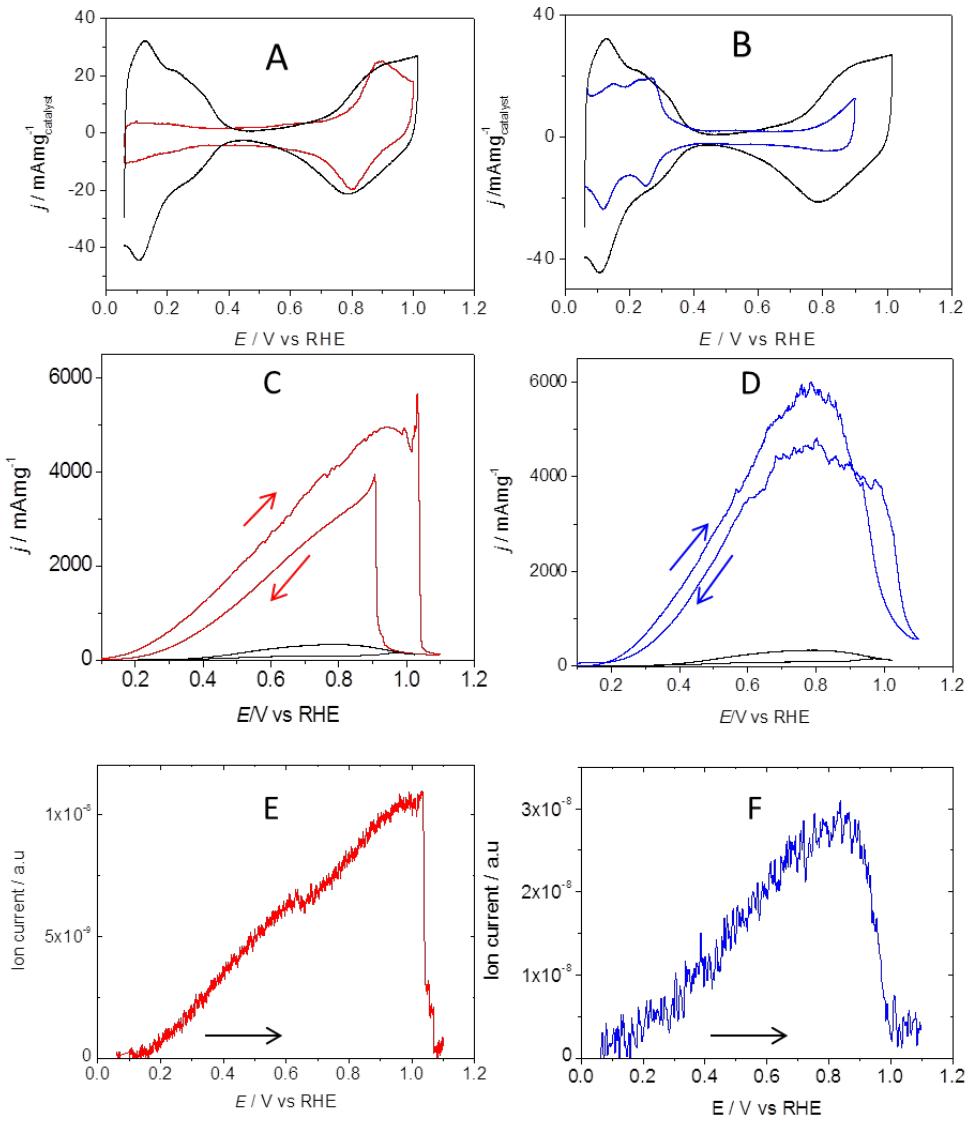

Figure 4. Voltammetric profiles of the $Pt_{70}Bi_{30}$ and $Pt_{90}Pb_{10}$ nanoparticles in (A) and (B) 0.5 M H_2SO_4 at υ= 50 mV/s ; (C) and (D) 0.5 M H_2SO_4 + 1 M HCOOH at υ= 10 mV/s . (E) and (F) Ion/mass current= 44 (CO_2) of the $Pt_{70}Bi_{30}$ and $Pt_{90}Pb_{10}$ nanoparticles in 0.5 M H_2SO_4 + 1 M HCOOH at υ= 10 mV/s.

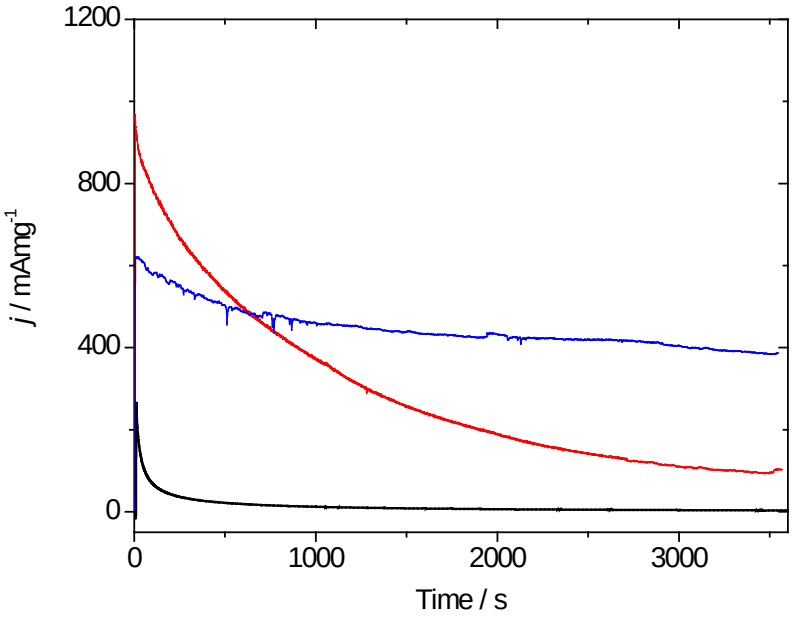

Figure 5. Chronoamperometries of $Pt_{90}Pb_{10}$ (blue) $Pt_{70}Bi_3$ (red) and Pt (black) nanoparticles for the formic acid oxidation at 0.3 V in 0.5 M H_2SO_4 + 1 M HCOOH at υ= 10 mV/s. The current density for the Pt nanoparticles was multiplied by 1000 for the sake of comparison.